Journal of Science: Advanced Materials and Devices 1 (2016) 393–399

Contents lists available at ScienceDirect

Journal of Science: Advanced Materials and Devices

journal homepage: www.elsevier.com/locate/jsamd

Original Article

A tunable multiband chirped metasurface

Libang Mao, Tun Cao*

Department of Biomedical Engineering, Faculty of Electronic Information and Electrical Engineering, Dalian University of Technology, People's Republic of China

ARTICLE INFO

Article history:
Received 17 June 2016
Received in revised form
17 July 2016
Accepted 17 July 2016
Available online 22 July 2016

Keywords:
Tunable
Metamaterials
Surface plasmon resonance
Chirp
Negative refraction

ABSTRACT

We numerically present a multiband double negative chirped metasurface (MS) in the near-infrared (N-IR) region. The MS was composed of a round nanoholes array (RNA) penetrating through metal/dielectric material/metal (Au–Al_2O_3–Au) trilayers. The chirp was excited by varying the positions of the RNA along the direction of incident electric (*E*) field vector inside the meta-atom. It is found that besides a multi-band double negative refractive index (NRI), a spectral tuning of NRI is also unveiled by moving the neighbouring round holes closer to each other. Importantly, we also show that the chirped MS with large round hole resonators possesses a high value of the Figure-of-Merit (FOM) in the optical region.

1. Introduction

Materials with negative refraction, also known as left-handed materials, have attracted intensive attention nowadays. Such a negative refractive index (NRI) material was first predicted in 1967 [1]. In the last decade, this theoretical curiosity was experimentally validated by fabricating patterned metallic structures consisting of metallic wires and split-ring resonators [2,3], so called meta-mateirals (MMs). This results in a rapid progress in various aspects of NRI MMs, seeking simple structures and interesting applications [4–6]. Particularly, many new physical phenomena unavailable in nature using the MMs have been predicted, such as the fundamental concept of perfect lens [7] and cloaking [8–10]. One of the important designs for the NRI material is composite periodic structures made of air holes embedded through alternating layers of metal and dielectric, so called fishnet MMs [11–13]. The exotic electromagnetic (EM) properties of the multilayer fishnet MM strongly depend on the geometry of the meta-atoms, which is due to the plasmonic waveguide modes stemming from surface plasmon polaritons (SPPs) [14]. Such a fishnet MM demonstrates many intriguing properties, for example it shows that incident light can couple to different orders of SPP modes through the holes to excite multiple magnetic dipolar moments and thus results in multiband NRI MMs [15].

In particular, a series of recent studies revealed the existence of dual-band NRI material associated with the fishnet structures. A strategy of two fishnet magnetic resonators with different dimensions was taken to obtain a dual-band NRI [16]. Although it provides a double negative index (low loss) in the N-IR region, it is limited by a single negative (high loss) index in the middle-infrared (M-IR) region. The fishnet MMs composed of alternating layers of metal and dielectric were proposed to achieve a dual-band double negative index in the visible region [15], whereas the multilayer design complicates the fabrication. In contrast, MM based on a single layer also showed its potential of obtaining the dual-band NRI, where the high-order resonance is controlled by means of substrate properties [17]. However, they only demonstrated the dual-band double negative index (DNI) in the subterahertz range. Moreover, the integration of the required MM structures and the electrodes etc. for tuning active dielectric substrate may be challenge. Afterwards, a MM composed of hexagonal arrays of triangular penetrating through metal-dielectric-metal laminates was demonstrated, where the two asymmetric hybridized plasmon modes provide a dual-band optical NRI [18]. Nevertheless, this structure only exhibits double negative MMs in one band (the lower frequency region) and their studies may be more reasonable if the fabrication process can be simplified. A dual-band DNI material was also achieved using symmetric fishnet MMs penetrated through metal/dielectric/metal (MDM) trilayers [19,20]. However,

* Corresponding author.
E-mail address: caotun1806@dlut.edu.cn (T. Cao).
Peer review under responsibility of Vietnam National University, Hanoi.

http://dx.doi.org/10.1016/j.jsamd.2016.07.004

small holes need to be employed in order to attain negative permeability in the dual band that leads to a low Figure-of-Merit (FOM) [21].

In this work, we demonstrate a chirped metasurface (MS) formed by a round nanohole array (RNA) perforating through a MDM trilayer. The chirp is introduced by moving the neighbouring round holes towards each other from their central positions. We show that such a structure can provide a NRI with simultaneous negative permittivity and permeability in the two different optical regions (visible and N-IR). Whilst by moving the neighbouring round holes closer to each other, we observe a spectral red-shift of the NRI with a reduced magnetic resonance in the visible region and red-shift with an increased magnetic resonance in the N-IR region. Noteworthy, different from the previous reports, our strategy doesn't require for small apertures hence has the advantage of attaining the NRI with high FOMs in both visible and N-IR regions. This dual-band double negative chirped MS exhibits a simple profile which remains compatible with standard fabrication techniques. It is of great importance to realize high performance, active metamaterials for a wide range of impactful optical applications such as spectroscopy, ellipsometry and imaging.

2. Materials and methods

The normal symmetric fishnet MS are trilayer structures made of two 30 nm thick Au layers spaced by a 60 nm thick Al_2O_3 dielectric interlayer with an inter-penetrating two dimensional square array of round holes shown in Fig. 1(a,b). In Fig. 1(c,d), a chirped fishnet MS is created by simultaneously displacing rows 1 and 2, and rows 3 and 4 towards each other from their centers with a distance "δ". The unit cell is shown in Fig. 1(b,d) for both normal and chirped MSs respectively, where the pitch of the RNA, $L = 400$ nm, L_{x1} and L_{x2} are the chirped lattice constants along the direction of the incident E-field vector, where $L_{x1} = L_x - 2\delta$ and $L_{x2} = L_x + 2\delta$, the diameter of the round holes is $d = 240$ nm which has been optimized to produce a high FOM, β is a cross-section plane of the structure. The z-axis is normal to the MS's surface and the x-y plane is parallel to the MS's surface. In order to simplify the model, the MSs are considered to be suspended in vacuum that can be achieved by a deep etching of a silicon support substrate. The unit cell is periodically extended along the x and y axes. The Au bottom layer interacts with the upper Au layer to provide a closed loop of displacement current (J_D) to excite strong magnetic resonances. Au is selected as the metal due to its stability and low ohmic loss. The dimension of the unit cell and the thickness of each layer are optimized to allow for the impedance matching between the MS and impinging plane wave [22]. The chirped MSs are simulated by a commercial software Lumerical FDTD Solutions based on the Finite-difference time-domain (FDTD) Method, where the S-parameters of reflection $r(\omega)$ and transmission $t(\omega)$ coefficients are obtained to retrieve the effective parameters for the chirped MS. The dielectric properties of Au as given by Johnson & Christy are used [23]. A plane wave is normally launched to the structure. The perfectly match layer and absorbing boundaries are applied along the z direction and periodic boundaries in the x–y plane. A uniform FDTD mesh size is adopted; the mesh size is the same along all Cartesian axes: $\Delta x = \Delta y = \Delta z = 2$ nm, which is sufficient to minimize the numerical errors arising from the FDTD method.

The impedance, η, and effective refractive index, n_{eff}, of the chirped MS are derived from the complex coefficients of reflection $r = R_a e^{i\phi_{ra}}$ and transmission $t = T_a e^{i\phi_a}$ by the Fresnel formula [24], where T_a is the amplitude and φ_a the phase of the transmission coefficient, R_a the amplitude and φ_{ra} the phase of the reflection coefficient. For an equivalent isotropic homogenous slab of thickness h surrounded by semi-infinite media with refractive index n_1 and n_3 under normal incidence, we have

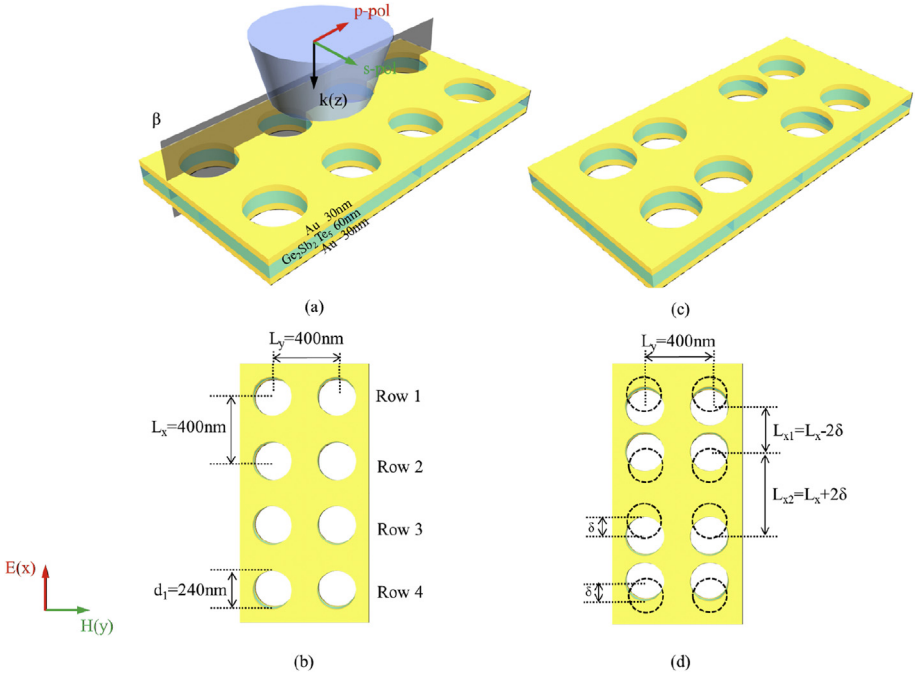

Fig. 1. (a) Schematic of the normal symmetric MSs exhibiting a 60 nm thick Al_2O_3 dielectric layer between two 30 nm thick Au films perforated with a square array of round holes suspended in a vacuum. The lattice constant is $L = 400$ nm and hole diameters are $d = 240$ nm. (b) Illustration of RNA lattice in a normal MS. (c) Schematic of the chirped MM consisting of a 60 nm thick Al_2O_3 dielectric layer between two 30 nm thick Au films perforated with a rectangular array of round holes suspended in a vacuum. The lattice constant along the y-direction is $L_y = 400$ nm, L_{x1} and L_{x2} are the chirped lattice constants along the x-direction, where $L_{x1} = L_x$-2δ and $L_{x2} = L_x$+2δ. (d) Illustration of RNA lattice in a chirped MM.

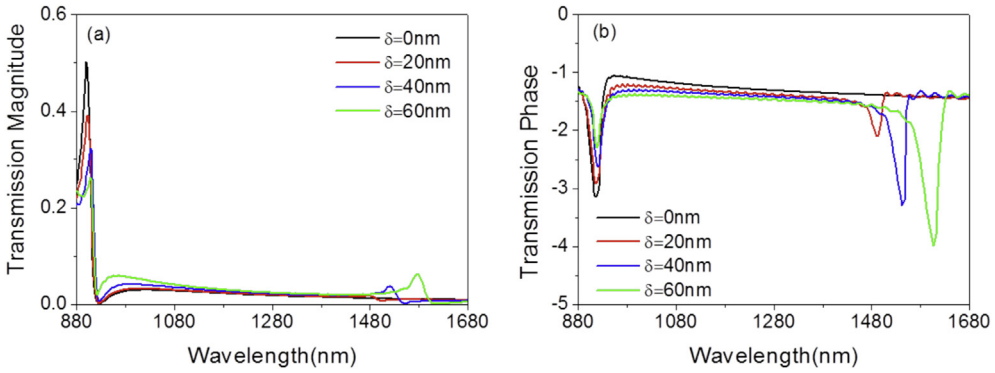

Fig. 2. 3D FDTD simulation of (a) transmission; (b) the real part of permeability of the chirped fishnet MM for the different values of δ at normal incidence.

$$\eta = \pm\sqrt{\frac{(1+r)^2 - t^2}{n_1^2(1+r)^2 - n_3^2 t^2}} \tag{1}$$

$$n_{eff} = \pm\frac{1}{kh}\arccos\left(\frac{1}{t}\frac{n_1(1-r^2)+n_3t^2}{n_1+n_3+r(n_3-n_1)}\right) + \frac{2\pi m}{kh} \tag{2}$$

The effective permittivity (ε_{eff}) and permeability (μ_{eff}) of the chirped MS are extracted using the well-known Nicholson-Ross-Weir (NRW) method [25,26]. Therefore, once refractive index (n_{eff}) and impedance (η) are evaluated, the effective permittivity and permeability can be calculated using

$$\varepsilon_{eff} = n_{eff}/\eta, \mu_{eff} = n_{eff}\eta \tag{3}$$

where, h is the thickness of the structure, $k = \omega/c$, c is the speed of light, m is an arbitrary integer and $n_1 = n_3 = 1$ since the structure is suspended in a vacuum. The signs of n_{eff} and η and the value of m are resolved by the passivity of metamaterial that requires the signs

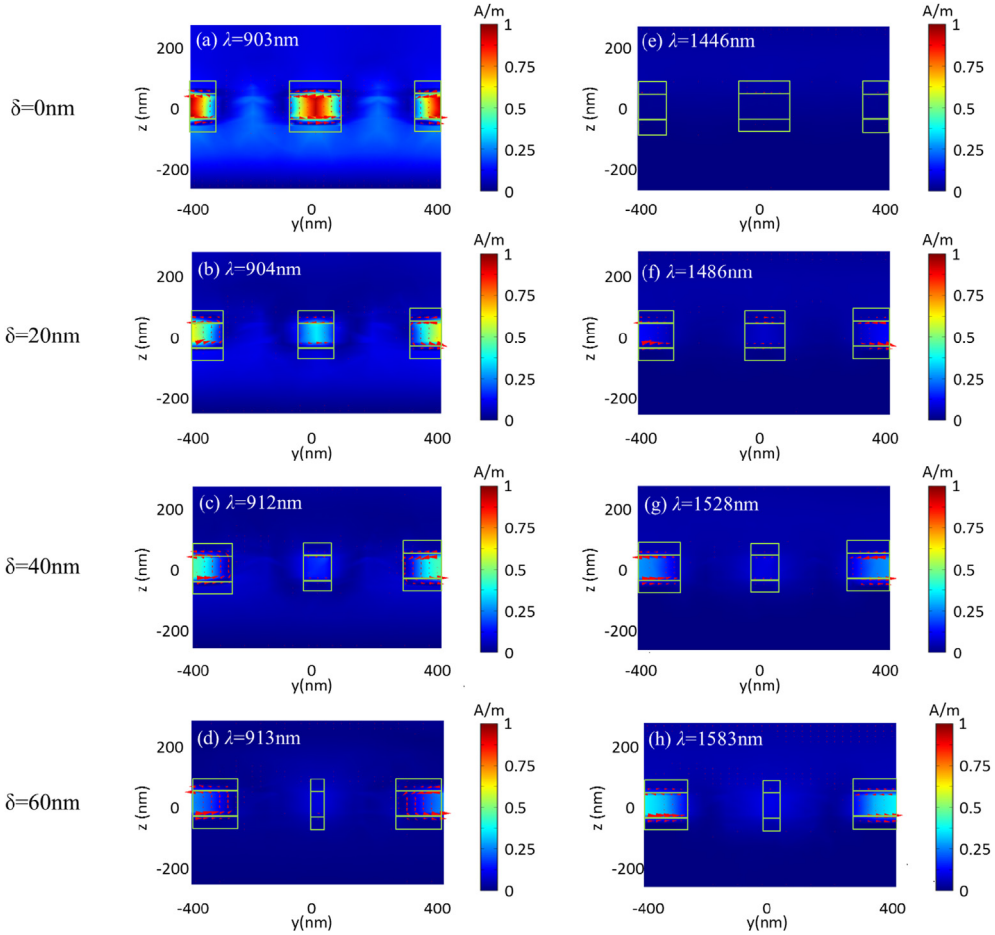

Fig. 3. 3D FDTD simulation of H-field distribution and J_D along β plane for the first resonance modes at (a) $\delta = 0$ nm, $\lambda = 903$ nm; (b) $\delta = 20$ nm, $\lambda = 904$ nm; (c) $\delta = 40$ nm, $\lambda = 912$ nm; (d) $\delta = 60$ nm, $\lambda = 913$ nm; for the second resonance modes at (e) $\delta = 0$ nm, $\lambda = 1446$ nm; (f) $\delta = 20$ nm, $\lambda = 1486$ nm; (g) $\delta = 40$ nm, $\lambda = 1528$ nm; (h) $\delta = 60$ nm, $\lambda = 1583$ nm.

of real part of impedance η and imaginary part of effective index n_{eff} are positive i.e. Real(η)>0, Imag(n_{eff}) > 0 which is consistent with the study described in [27,28]. This extraction approach is then applied to determine the variation in the optical response of the MS as the δ is changed. As shown in Fig. 1(a), the incident *E*-field is polarized along the *x*-direction.

3. Results and discussions

Fig. 2 shows the transmission of the chirped MSs at various δ respectively. Fig. 2(a) shows that two extraordinary optical transmissions (EOTs) can be excited if we modify the *x*-direction periodicity (L_{x1} and L_{x2}) of RNA by moving the neighbouring round holes towards each other from their centers (i.e., increase δ). These EOTs origin from the double magnetic resonances that can in turn contribute to a dual-band negative permeability shown in Fig. 7(a). As increasing δ, the transmission decreases and red-shifts in the first band (the visible region), whereas it increases and red-shifts in the second band (the N-IR region). Fig. 2(b) shows the phase of transmission coefficient. As can be seen, the transmission phase possesses a dip around the resonance, showing that the light is advanced in phase at the resonances, characteristic of a NRI material.

It has been demonstrated the electromagnetic interactions between the meta-atoms may influence MMs [29–32]. To further understand the underlying physics of the resonance

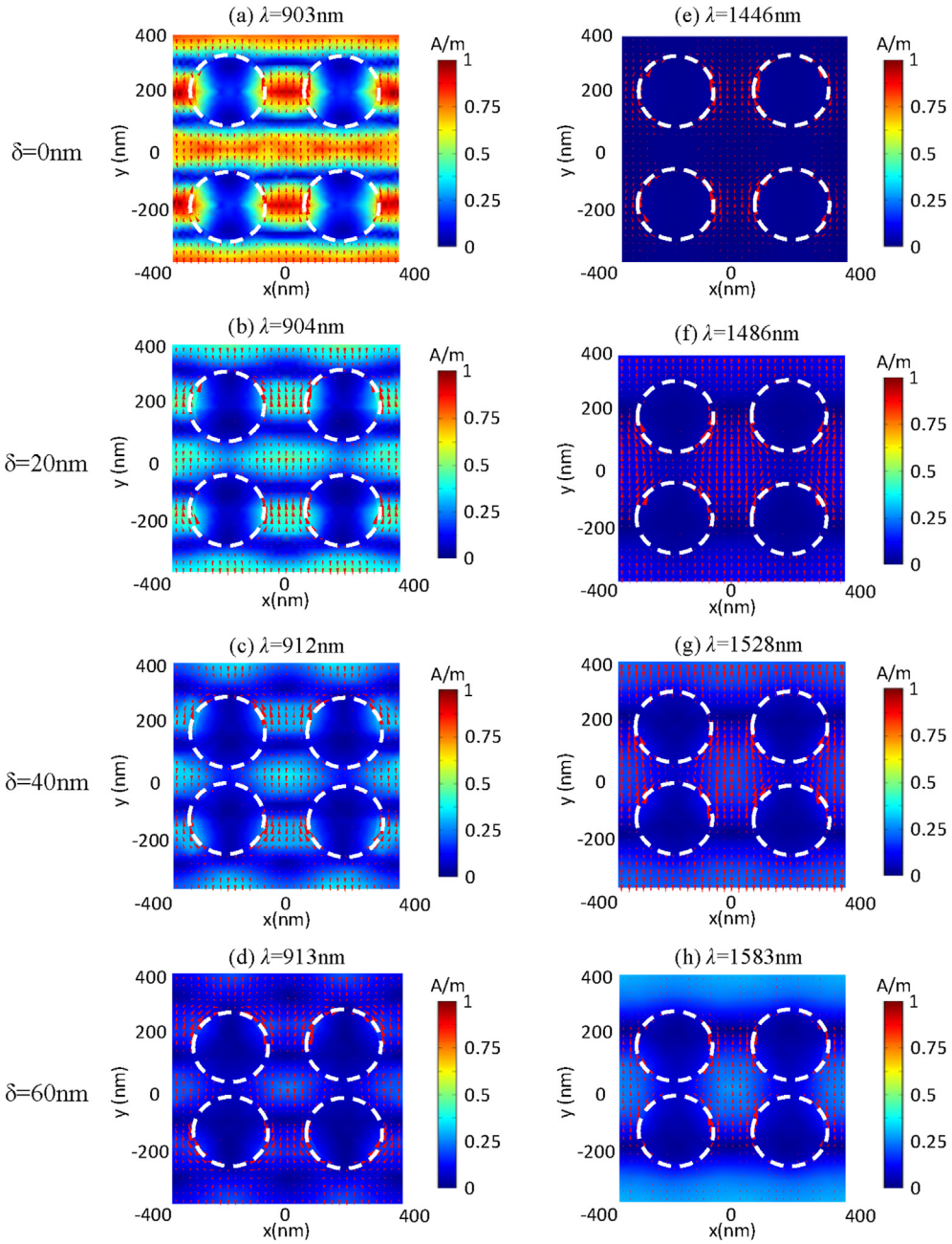

Fig. 4. 3D FDTD simulation of *H*-field distribution and surface currents along *x*–*y* plane for the first resonance modes at (a) δ = 0 nm, λ = 903 nm; (b) δ = 20 nm, λ = 904 nm; (c) δ = 40 nm, λ = 912 nm; (d) δ = 60 nm, λ = 913 nm; for the second resonance modes at (e) δ = 0 nm, λ = 1446 nm; (f) δ = 20 nm, λ = 1486 nm; (g) δ = 40 nm, λ = 1528 nm; (h) δ = 60 nm, λ = 1583 nm.

shifts, it is important to explore coupling effects between the round holes in our proposed MS. The electromagnetic coupling strength between the holes can be effectively improved when the holes are getting closer with increasing δ. As can be seen in Fig. 2, the spectra of transmission splits up because the coupling strength pronouncedly increases with δ [29,30]. For the second resonance mode, both the inductive and conductive couplings are improved due to the reduced distance, allowing for further increasing the coupling strength between the two round holes; however for the first resonance mode, the interaction between the two holes is only associated with inductive coupling [31,32]. Therefore, the first mode does not have prominent shifts than the second mode. This phenomenon is consistent with previous works [29–32].

The strong magnetic resonance origins from the loop of J_D. These J_D loops are excited by internal SPP modes flowing through the inner metal-dielectric interfaces of the structure [33,34]. To gain insight into the multiple magnetic resonances and the effect of δ in modulating the resonant modes, we simulate the total magnetic field (H) distribution for the structures with various δ of 0, 20, 40 and 60 nm, where $H = \sqrt{|H_x|^2 + |H_y|^2 + |H_z|^2}$. In Fig. 3, the arrows present currents whereas the colour present the magnitude of the H-field. For the structure with $\delta = 0$ nm, the displacement current J_D and H-field distribution for wavelengths of 903 nm, 904 nm, 912 nm, 913 nm in the first N-IR resonance region and wavelengths of 1446 nm, 1486 nm, 1528 nm, 1583 nm in the second M-IR resonance region are plotted along β-plane.

Fig. 3(a) shows the H-field at $\lambda = 903$ nm is efficiently concentrated in the Al_2O_3 dielectric interlayer, as expected for the internal SPP modes. Meanwhile, it shows the anti-parallel currents are excited at top and bottom internal Au interfaces, closed by J_D. Current loops between the Au layers are formed to excite the magnetic dipolar resonance of the negative permeability [20]. Nonetheless, the localized magnetic field intensity is extremely low and thus magnetic dipolar moment at $\lambda = 1446$ nm shown in Fig. 3(e). It presents that H-field intensity decreases for the first mode resonating in the N-IR region in Fig. 3(a)–(d) and increases for the second mode in the M-IR region in Fig. 3(e)–(h) by increasing the δ, which agrees well with the Real(μ_{eff}) (shown in Fig. 7(a)).

Fig. 4 shows the H-field intensities and surface currents in the x-y plane for the various δ. We present that H-field intensity in the x-y plane decreases for the first resonant mode in Fig. 4(a)–(d) and increases for the second resonant mode in Fig. 4(e)–(h) by increasing the δ. The distributions of the surface currents clearly show the existences of the magnetic dipolar resonances.

At the magnetic resonance, the structure is impedance matched and thus exhibits reflection dips shown in Fig. 5(a). As increasing δ, the magnitude of reflection increases and red-shifts in the first resonance band, but decreases and red-shifts in the second resonance band. Fig. 5(b) show the phase of reflection coefficients, which possesses a peak around the resonance, indicating that the light is advanced in phase at the resonances, characteristic of a NRI material.

Taking into account the thickness of the chirped MSs, Fig. 5 show the effective refractive index retrieved from transmission and reflection coefficients for the different δ. The bandwidth of the negative Real(n_{eff}) in Fig. 6(a) roughly matches the bandwidth of phase dip in Fig. 2(b). For different values of δ, the minimum values of the Real(n_{eff}) range from -3.2 to -2 for the first resonance mode and from 0 to -5.8 for the second resonance mode. Considering the losses, the *FOM* defined as $FOM = \text{Real}(n_{eff})/\text{Imag}(n_{eff})$ is used to show the overall performance of the MMs. As shown in Fig. 6(c), the *FOM* in the first resonance region attains the maximum ($FOM = 7.7$) at $\delta = 0$, which is high for the visible – N-IR range. This is because the large round apertures reduce the area of Au, thus decreasing the loss [11]. We then fix the size of the holes and increase δ. As can be seen, *FOM* decreases with δ in the first resonance region whereas increases with δ in the second band. Nevertheless, *FOM* still have the value of 2.9 at $\lambda = 913$ nm and 1.8 at $\lambda = 1583$ nm for $\delta = 60$ nm. Furthermore, in both of the resonance bands, for a considerable wavelength range, the *FOM* is larger than one. Therefore, our proposed chirped MS can possess a dual band double negative index with low losses. Notably, the *FOM* can be further improved by integrating gain materials into the chirped MS [35–37].

Fig. 7 shows the μ_{eff} and ε_{eff} at different δ. It can be seen that the EOT windows overlap with the frequency regions where negative Real(μ_{eff}) and Real(ε_{eff}) coincide (see Fig. 7(a,c)), enabling a dual-band double negative MS. For the frist resonance mode, the absolute value of negative Real(μ_{eff}) decreases because the magnetic resonance is attenuated by increasing δ, shown in Fig. 3(a)–(d). However, for the second resonance mode, the absolute value of negative Real(μ_{eff}) increases with δ, due to the increasing magnetic resonance in the MS, shown in Fig. 3(e)–(h).

4. Conclusion

We have numerically proposed a chirped fishnet metasurface composed of round circular holes embedding through the metal/dielectric/metal trilayers. We have considered the chirp

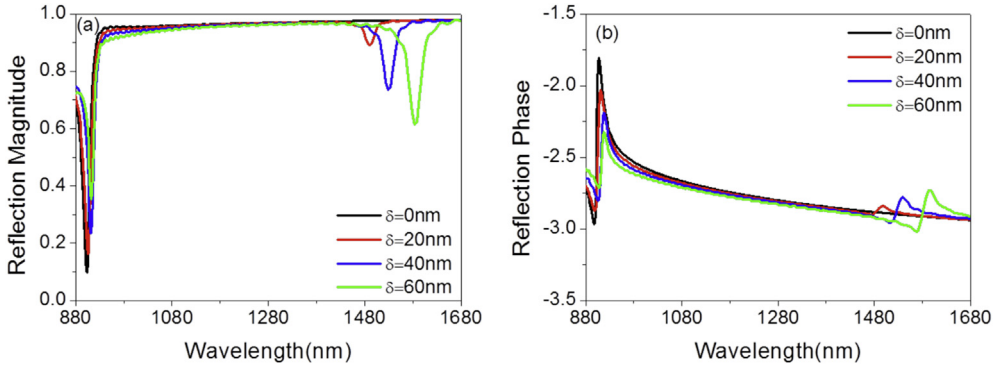

Fig. 5. 3D FDTD simulation of (a) transmission magnitudes; (b) reflection magnitudes; (c) transmission phases; (d) reflection phases for different δ under normal incidence.

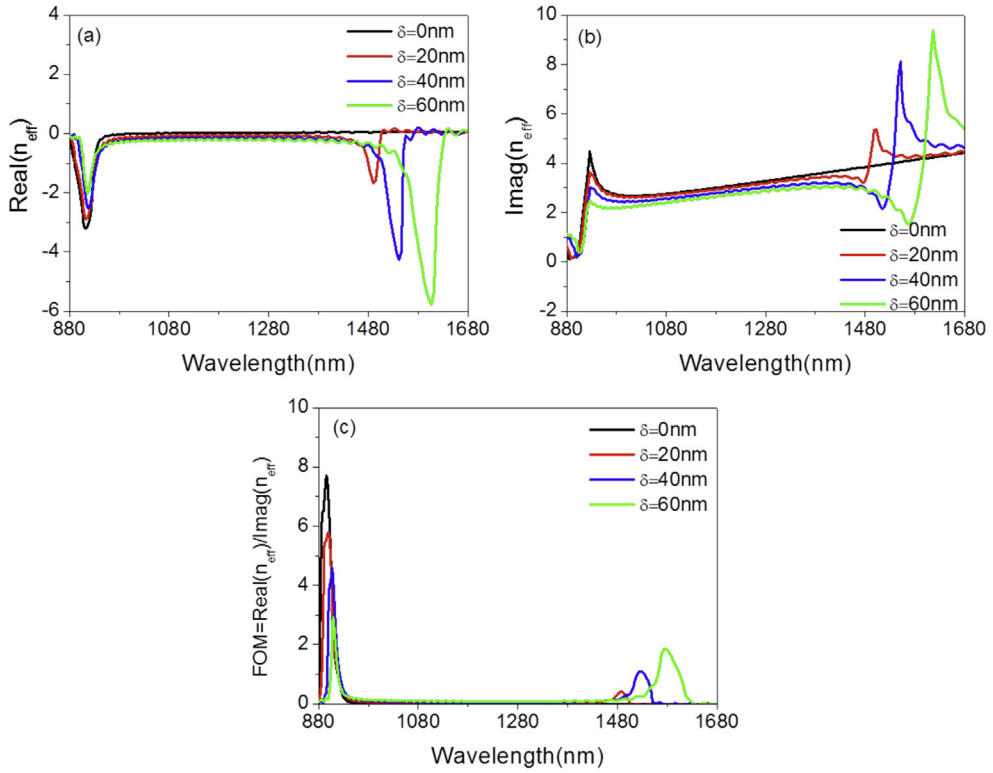

Fig. 6. 3D FDTD simulation of (a) real part of n_{eff}; (b) imaginary part of n_{eff}; (c) figure-of-merit for different values of δ for p-polarization at normal incidence angle.

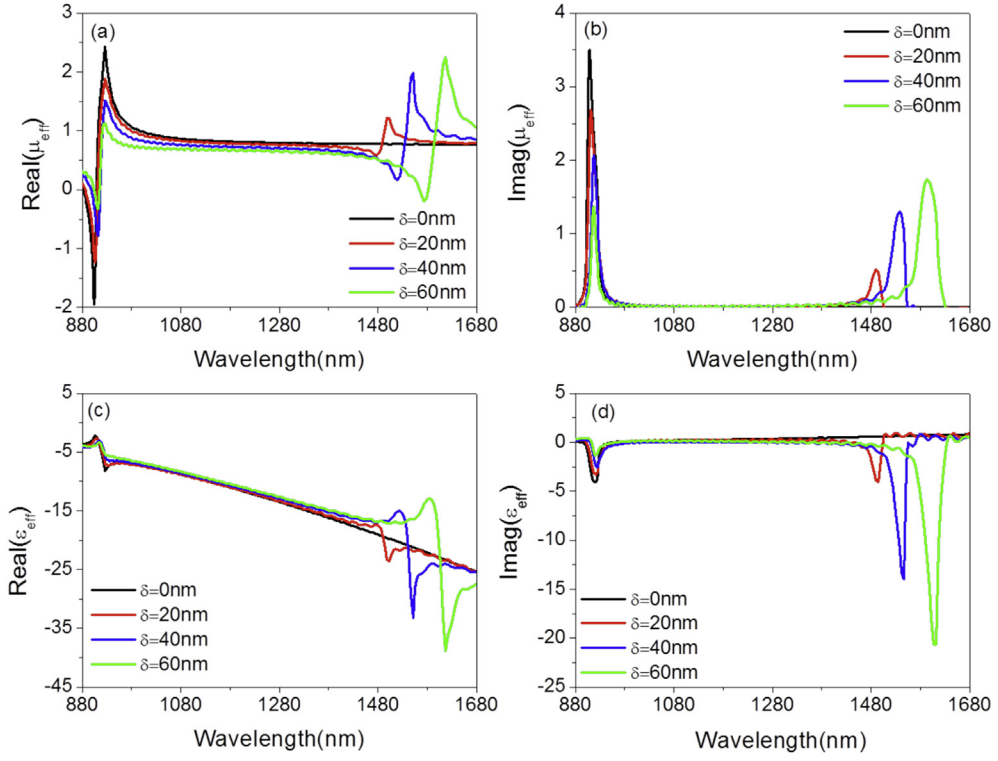

Fig. 7. 3D FDTD simulation of (a) real part of permeability; (b) imaginary part of permeability; (c) real part of permittivity; (d) imaginary part of permittivity for different values of δ under normal incidence.

parameters in the structure introduced by displacing the neighbouring circular holes closer to each other along the x-direction inside the unit cell. By increasing the δ, we have provided a chirped metasurface exhibiting two wavelength regions of double negative index, one around the visible region and the other in the N-IR region, and have found the variation of δ can significantly effect the strengths and wavelength positions of the SPP modes. Importantly, such a chirped metasurface possesses a high *FOM* in

the optical region attributed to the large size of the meta-atom (i.e. round holes). Moreover, our structure possesses an uncomplicated geometry that remains compatible with standard lithographic patterning and can be easily fabricated in the optical region.

Acknowledgements

We acknowledge the financial support from National Natural Science Foundation of China (Grant Nos. 61172059, 51302026), International Science & Technology Cooperation Program of China (Grant No.2015DFG12630) and Program for Liaoning Excellent Talents in University (Grant No. LJQ2015021).

References

[1] V.G. Veselago, Properties of materials having simultaneously negative values of the dielectric (ε) and the magnetic (μ) susceptibilities, Sov. Phys. Solid State 8 (1967) 2854.
[2] D.R. Smith, J.B. Pendry, M.C.K. Wiltshire, Metamaterials and negative refractive index, Science 305 (2004) 788. http://science.sciencemag.org/content/305/5685/788.
[3] R.A. Shelby, D.R. Smith, S. Shultz, Experimental verification of a negative index of refraction, Science 292 (2001) 77. http://science.sciencemag.org/content/292/5514/77.
[4] C.W. Qiu, L. Gao, Resonant light scattering by small coated nonmagnetic spheres: magnetic resonances, negative refraction, and prediction, J. Opt. Soc. Am. B 25 (2008) 1728–1737. https://www.osapublishing.org/abstract.cfm?uri=josab-25-10-1728.
[5] V.M. Shalaev, Optical negative-index metamaterials, Nat. Photonics 1 (2007) 41–48. http://www.nature.com/nphoton/journal/v1/n1/abs/nphoton.2006.49.html.
[6] C.M. Soukoulis, M. Wegener, Past achievements and future challenges in the development of three-dimensional photonic metamaterials, Nat. Photonics 5 (2011) 523–530. http://www.nature.com/nphoton/journal/v5/n9/abs/nphoton.2011.154.html.
[7] J.B. Pendry, Negative refraction makes a perfect lens, Phys. Rev. Lett. 85 (2000) 3966. http://journals.aps.org/prl/abstract/10.1103/PhysRevLett.85.3966.
[8] J.B. Pendry, D. Schurig, D.R. Smith, Controlling electromagnetic fields, Science 312 (2006) 1780. http://science.sciencemag.org/content/312/5781/1780.
[9] D. Schurig, J.J. Mock, B.J. Justice, S.A. Cummer, J.B. Pendry, A.F. Starr, D.R. Smith, Metamaterial electromagnetic cloak at microwave frequencies, Science 314 (2006) 977. http://science.sciencemag.org/content/314/5801/977.short.
[10] U. Leonhardt, Optical conformal mapping, Science 312 (2006) 1777. http://science.sciencemag.org/content/312/5781/1777.
[11] S. Zhang, W. Fan, N.C. Panoiu, K.J. Malloy, R.M. Osgood, S.R.J. Brueck, Experimental demonstration of near-infrared negative-index metamaterials, Phys. Rev. Lett. 95 (2005) 137404. http://journals.aps.org/prl/abstract/10.1103/PhysRevLett.95.137404.
[12] U.K. Chettiar, A.V. Kildishev, H.K. Yuan, W. Cai, S. Xiao, V.P. Drachev, V.M. Shalaev, Dual-band negative index metamaterial: double negative at 813nm and single negative at 772nm, Opt. Lett. 32 (2007) 1671–1673. https://www.osapublishing.org/ol/abstract.cfm?uri=ol-32-12-1671.
[13] C. García-Meca, R. Ortuño, F.J. Rodríguez-Fortuño, J. Martí, A. Martínez, Double-negative polarization-independent fishnet metamaterial in the visible spectrum, Opt. Lett. 34 (2009) 1603–1605. https://www.osapublishing.org/ol/abstract.cfm?uri=ol-34-10-1603.
[14] T. Paul, C. Menzel, C. Rockstuhl, F. Lederer, Advanced optical metamaterials, Adv. Mater 22 (2010) 2354–2357. http://onlinelibrary.wiley.com/doi/10.1002/adma.200903865/full.
[15] M.I. Aslam, D.Ö. Güney, Dual-band, double-negative, polarization-independent metamaterial for the visible spectrum, J. Opt. Soc. Am. B 29 (2012) 2839–2847. https://www.osapublishing.org/abstract.cfm?uri=josab-29-10-2839.
[16] D.H. Kwon, D.H. Werner, A.V. Kildishev, V.M. Shalaev, Near-infrared metamaterials with dual-band negative-index characteristics, Opt. Express 15 (2007) 1647–1652. https://www.osapublishing.org/abstract.cfm?uri=oe-15-4-1647.
[17] C. Sabah, H.G. Roskos, Dual-band polarization-independent sub-terahertz fishnet metamaterial, Curr. Appl. Phys. 12 (2012) 443–450. http://www.sciencedirect.com/science/article/pii/S1567173911004329.
[18] M. Giloan, S. Astilean, Dual-band optical negative index metamaterial based on hexagonal arrays of triangular nanoholes in metal-dielectric films, Opt. Commun. 296 (2013) 141–148. http://www.sciencedirect.com/science/article/pii/S0030401813001454.
[19] K.M. Dani, Z. Ku, P.C. Upadhya, R.P. Prasankumar, A.J. Taylor, S.R.J. Brueck, Ultrafast nonlinear optical spectroscopy of a dual-band negative index metamaterial all-optical switching device, Opt. Express 19 (2011) 3973–3983. https://www.osapublishing.org/abstract.cfm?uri=oe-19-5-3973.
[20] T. Cao, M.J. Cryan, Study of incident angle dependence for dual-band double negative-index material using elliptical nanohole arrays, J. Opt. Soc. Am. A 29 (2012) 209–215. https://www.osapublishing.org/josaa/abstract.cfm?uri=josaa-29-3-209.
[21] S. Zhang, W. Fan, K.J. Malloy, S.R.J. Brueck, N.C. Panoiu, R.M. Osgood, Near-infrared double negative metamaterials, Opt. Express 13 (2005) 4922–4930. https://www.osapublishing.org/oe/abstract.cfm?uri=oe-13-13-4922.
[22] J. Carbonell, C. Croënne, F. Garet, E. Lheurette, J.L. Coutaz, D. Lippens, Lumped elements circuit of terahertz fishnet-like arrays with composite dispersion, J. Appl. Phys. 108 (2010) 014907. http://scitation.aip.org/content/aip/journal/jap/108/1/10.1063/1.3455994.
[23] P.B. Johnson, R.W. Christy, Optical constants of noble metals, Phys. Rev. B 6 (1972) 4370–4379. http://journals.aps.org/prb/abstract/10.1103/PhysRevB.6.4370.
[24] M. Born, E. Wolf, A.B. Bhatia, Principles of Optics, Cambridge University Press, Cambridge, 1997.
[25] R.W. Ziolkowski, Design, fabrication and testing of double negative metamaterials, IEEE Trans. Antennas Propag. 51 (2003) 1516–1529. http://ieeexplore.ieee.org/xpls/abs_all.jsp?arnumber=1210783.
[26] A.M. Nicolson, G.F. Ross, Measurement of intrinsic properties of materials by time-domain techniques, IEEE Trans. Instrum. Meas. 19 (1970) 377–382. http://ieeexplore.ieee.org/xpls/abs_all.jsp?arnumber=4313932.
[27] D.R. Smith, S. Schultz, P. Markos, C.M. Soukoulis, Determination of effective permittivity and permeability of metamaterials from reflection and transmission coefficients, Phys. Rev. B 65 (2002) 195104. http://journals.aps.org/prb/abstract/10.1103/PhysRevB.65.195104.
[28] X.D. Chen, T.M. Grzegorczyk, B. Wu, J. Pacheco Jr., J.A. Kong, Robust method to retrieve the constitutive effective parameters of metamaterials, Phys. Rev. E 70 (2004) 016608. http://journals.aps.org/pre/abstract/10.1103/PhysRevE.70.016608.
[29] N. Liu, S. Kaiser, H. Giessen, Magnetoinductive and electroinductive coupling in plasmonic metamaterial molecules, Adv. Mater 20 (2008) 4521–4525. http://onlinelibrary.wiley.com/doi/10.1002/adma.200801917/full.
[30] N. Liu, H. Giessen, Coupling effects in optical metamaterials, Angew. Chem. Int. Ed. 49 (2010) 9838–9852. http://onlinelibrary.wiley.com/doi/10.1002/anie.200906211/full.
[31] H. Liu, D.A. Genov, D.M. Wu, Y.M. Liu, J.M. Steele, C. Sun, S.N. Zhu, X. Zhang, Magnetic plasmon propagation along a chain of connected subwavelength resonators at infrared frequencies, Phys. Rev. Lett. 97 (2006) 243902. http://journals.aps.org/prl/abstract/10.1103/PhysRevLett.97.243902.
[32] N. Wongkasem, A. Akyurtlu, K.A. Marx, Q. Dong, J. Li, W.D. Goodhue, Development of chiral negative refractive index metamaterials for the terahertz frequency regime, IEEE Trans. Antennas Propag. 55 (2007) 3052. http://ieeexplore.ieee.org/xpl/freeabs_all.jsp?arnumber=4380591&reason=concurrency.
[33] A. Mary, S.G. Rodrigo, F.J. Garcia-Vidal, L. Martin-Moreno, Theory of negative-refractive-index response of double-fishnet structures, Phys. Rev. Lett. 101 (2008) 103902. http://journals.aps.org/prl/abstract/10.1103/PhysRevLett.101.103902.
[34] R. Ortuño, C. García-Meca, F.J. Rodríguez-Fortuño, J. Martíand, A. Martínez, Role of surface plasmon polaritons on optical transmission through double layer metallic hole arrays, Phys. Rev. B 79 (2009) 075425. http://journals.aps.org/prb/abstract/10.1103/PhysRevB.79.075425.
[35] S. Xiao, V.P. Drachev, A.V. Kildishev, X. Ni, U.K. Chettiar, H. Yuan, V.M. Shalaev, Loss-free and active optical negative-index metamaterials, Nature 466 (2010) 735–738. http://www.nature.com/nature/journal/v466/n7307/abs/nature09278.html.
[36] A. Fang, Th Koschny, M. Wegener, C.M. Soukoulis, Self-consistent calculation of metamaterials with gain, Phys. Rev. B 79 (2009) 241104(R). http://journals.aps.org/prb/abstract/10.1103/PhysRevB.79.241104.
[37] A. Fang, Z. Huang, T. Koschny, C.M. Soukoulis, Overcoming the losses of a split ring resonator array with gain, Opt. Express 19 (2011) 12688–12699. https://www.osapublishing.org/abstract.cfm?uri=oe-19-13-12688.